



HAL
open science

Multiple transition zone seismic discontinuities and low velocity layers below western United States

Benoit Tauzin, Robert D. van Der Hilst, Gérard Wittlinger, Yanick Ricard

► **To cite this version:**

Benoit Tauzin, Robert D. van Der Hilst, Gérard Wittlinger, Yanick Ricard. Multiple transition zone seismic discontinuities and low velocity layers below western United States. *Journal of Geophysical Research: Solid Earth*, 2013, 118, pp.2307-2322. 10.1002/jgrb.50182 . hal-00853673

HAL Id: hal-00853673

<https://hal.science/hal-00853673>

Submitted on 18 Nov 2013

HAL is a multi-disciplinary open access archive for the deposit and dissemination of scientific research documents, whether they are published or not. The documents may come from teaching and research institutions in France or abroad, or from public or private research centers.

L'archive ouverte pluridisciplinaire **HAL**, est destinée au dépôt et à la diffusion de documents scientifiques de niveau recherche, publiés ou non, émanant des établissements d'enseignement et de recherche français ou étrangers, des laboratoires publics ou privés.

Multiple transition zone seismic discontinuities and low velocity layers below western United States

B. Tauzin,¹ R. D. van der Hilst,² G. Wittlinger,³ and Y. Ricard¹

Received 8 January 2013; revised 2 April 2013; accepted 4 April 2013; published 24 May 2013.

[1] With P-to-S converted waves recorded at seismic stations of the U.S. Transportable Array, we image the fine structure of upper mantle and transition zone (TZ) beneath the western U.S. We map the topographies of seismic discontinuities by stacking data by common conversion points along profiles. Systematic depth and amplitude measurements are performed not only for the well-known “410” and “660” interfaces but also for minor seismic discontinuities identified around 350, 590, and 630 km depths. The amplitude of conversion suggests shear wave velocity (V_s) increase by 4% at the 410 and the 660. The observed 660 velocity contrast is smaller than expected from the 6% in IASP91 but consistent with a pyrolytic model of mantle composition. The Gorda plate, subducted under northern California, is tracked to the TZ where it seems to flatten and induce uplift of the 410 under northern Nevada. Maps of 410/660 amplitude/topography reveal that the TZ is anomalous beneath the geographical borders of Washington, Oregon, and Idaho, with (1) a thickened TZ, (2) a sharp change in depth of the 660, (3) a reduced 410 conversion amplitude in the North, and (4) a positive “630” discontinuity. Such anomalous structure might be inherited from the past history of plate subduction/accretion. A thinned TZ under the Yellowstone suggests higher-than-average temperatures, perhaps due to a deep thermal plume. Both the “350” and the “590” negative discontinuities extend over very large areas. They might be related either to an increased water content in the TZ, a significant amount of oceanic material accumulated through the past 100 Myr, or both.

Citation: Tauzin, B., R. D. van der Hilst, G. Wittlinger, and Y. Ricard (2013), Multiple transition zone seismic discontinuities and low velocity layers below western United States, *J. Geophys. Res. Solid Earth*, 118, 2307–2322, doi:10.1002/jgrb.50182.

1. Introduction

[2] Seismic discontinuities near 410 km (the “410”) and 660 km depth (the “660”), bounding the transition zone (TZ), are usually attributed to solid-state phase changes in the mantle olivine components (respectively, olivine to wadsleyite and ringwoodite to perovskite + ferropericline). Weaker (and laterally intermittent) velocity gradients in the TZ are often associated with the wadsleyite to ringwoodite transformation near 520 km depth (the “520”) or with non-olivine transformations in garnet and pyroxene components [see *Ita and Stixrude*, 1992; *Vacher et al.*, 1998;

Weidner and Wang, 1998]. Seismological constraints on these discontinuities are usually discussed by exploring a reference pressure-temperature (P , T) phase diagram for a fixed bulk mantle composition and interpreted in terms of temperature [*Helffrich*, 2000]. However, compositional heterogeneities can add complexity to the discontinuity structure within or near the TZ.

[3] An example of such compositional heterogeneity is the supply of basaltic material to the mantle via subduction. Buried into the mantle, the subducted oceanic crust undergoes a sequence of phase transformations [*Irifune and Ringwood*, 1993; *Ricard et al.*, 2005] at depths different than those in the ambient mantle.

[4] Water in the TZ, possibly inherited from Earth’s formation [*Kawamoto et al.*, 1996] and reinforced via subduction of water-rich sediments [*Irifune et al.*, 1998], is another example of compositional heterogeneity affecting mantle discontinuities. Hydration reduces shear wave velocities [*Smyth and Jacobsen*, 2006] and can affect the coexistence domain of mineral assemblages during transformations, increasing the thickness of the 410, sharpening the 520, or deepening the 660 [e.g., *Wood*, 1995; *Higo et al.*, 2001; *Litasov et al.*, 2005a].

[5] The presence of volatile elements in Earth possibly decreases the wet solidus temperature to below the

¹Laboratoire de Géologie de Lyon, Terre, Planètes, Environnement, Université de Lyon1, CNRS et Ecole Normale Supérieure de Lyon, Villeurbanne, France.

²Department of Earth, Atmospheric, and Planetary Sciences, Massachusetts Institute of Technology, Cambridge, Massachusetts, USA.

³Institut de Physique du Globe de Strasbourg, Ecole et Observatoire des Sciences de la Terre, CNRS et Université de Strasbourg, Strasbourg, France.

Corresponding author: B. Tauzin, Laboratoire de Géologie de Lyon, Terre, Planètes, Environnement, Université Lyon 1, Université de Lyon, CNRS UMR 5276, 2 rue Raphaël Dubois, 69622 Villeurbanne Cedex, France. (benoit.tauzin@univ-lyon1.fr)

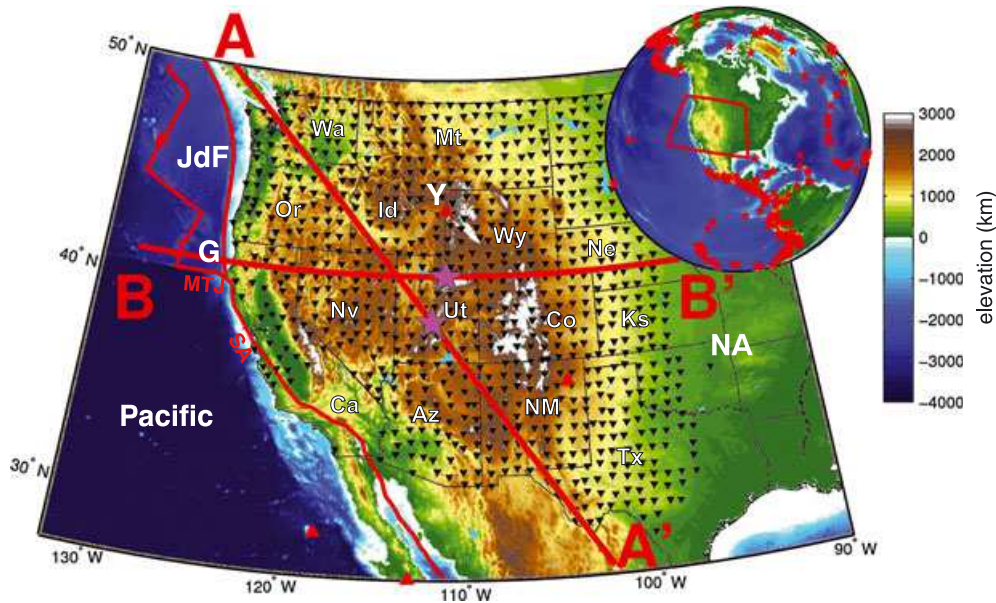


Figure 1. Map of western U.S. and the 820 U.S. Transportable Array broadband seismic stations (black triangles) used in this study. Red triangles are the locations of hot spots given by *Anderson and Schramm* [2005]. The plate boundaries of North America, Gorda-Juan de Fuca, and Pacific plates are contoured in red. The A-A' and B-B' profiles are used for common conversion point stacking of the data (Figures 3 and 4). Purple stars locate the middle of the profiles. NA: North American plate; JdF: Juan de Fuca plate; G: Gorda plate; Y: Yellowstone; MTJ: Mendocino Triple Junction; SA: San Andreas fault; Ca: California; Or: Oregon; Wa: Washington; Nv: Nevada; Id: Idaho; Az: Arizona; Ut: Utah; NM: New Mexico; Co: Colorado; Wy: Wyoming; Mt: Montana; Ne: Nebraska; Ks: Kansas; Tx: Texas. The inset shows the distribution of recorded seismicity.

geotherm. This may initiate partial melting even without anomalously high temperatures. Water-induced partial melting (the transition zone water filter model) [Bercovici and Karato, 2003] has been proposed to explain the presence of a low velocity layer atop the 410 [Revenaugh and Sipkin, 1994]. The sharp reduction of velocity at the onset of this layer is sometimes referred to as the “350” discontinuity [Vinnik and Farra, 2007]. Recent efforts established a global presence of the 350 at a global scale [Vinnik and Farra, 2007; Tauzin et al., 2010], with the distance above the 410 discontinuity changing laterally from 20 km to as much as 90 km over a few hundred kilometers. Correlations of these variations with hot [Vinnik and Farra, 2007] or cold [Song et al., 2004; Courtier and Revenaugh, 2007] tectonic environments remain elusive [Tauzin et al., 2010], suggesting that the variations in position cannot be explained by temperature alone [Song et al., 2004; Tauzin et al., 2010; Schmandt et al., 2011].

[6] The study of *Tauzin et al.* [2010] was at relatively low resolution owing to sparse data coverage on the global scale, and better characterization of the fine mantle discontinuity structure is possible at a regional scale. Here we study the western U.S. because dense arrays of seismic stations, constituting the Transportable Array component of USArray, have been recording passive seismicity since 2004 (Figure 1) and because low-velocity layers have been reported beneath some geographical regions. These include the border between Oregon and Washington [Song et al., 2004], Yellowstone [Fee and Dueker, 2004], the northern Rocky

Mountains [Jasbinsek and Dueker, 2007], the southern Colorado Plateau and the Rio Grande Rift [Jasbinsek et al., 2010], and under California [Vinnik et al., 2010].

[7] As in *Tauzin et al.* [2008, 2010], we use conversions from compressional to shear waves (P-to-S) to image mantle interfaces. Several studies have used similar data and methods to image the TZ structure below western U.S. [e.g., Eager et al., 2010; Cao and Levander, 2010; Schmandt et al., 2012a], and our main purpose is not to deliver new maps of the major TZ discontinuities but to use them to calibrate our technique and focus on the weaker signals associated with minor seismic discontinuities.

[8] North America (NA) has been shaped by the interaction of different subduction systems. The Pacific and some fragments of the old oceanic Farallon plate (the Gorda-Juan de Fuca plate) still exist today (Figure 1) whereas other oceanic plates have entirely disappeared [Lithgow-Bertelloni and Richards, 1998; Ren et al., 2007]. The style of subduction, with trench retreat and draping at the TZ, has evolved through time. From Cretaceous to early Eocene (ca. 80–40 Ma), low-angle subduction of the Farallon plate along the western margin of NA produced an intense phase of crustal shortening, uplift, and lithosphere modification, the Laramide orogeny, that propagated far inland by contrast with the preceding development of the Sevier fold thrust belt. Around 50 Ma, this subduction shifted further west, off the coasts of northern Oregon and Washington. The steep subduction of the Gorda-Juan de Fuca plate initiated the Cascade volcanic arc which is

still active today. After the Laramide orogeny, the western U.S. experienced widespread extensional tectonics in the Basin and Range province [Zoback *et al.*, 1981]. This intense stretching (WNW-ESE since 15 Ma) was associated with large upwelling and warming of the mantle, possibly due to the removal of the Farallon slab [e.g., Humphreys, 1995]. The extension was accompanied by widespread ignimbrite magmatism. More recent episodes of active volcanism occurred, with the flare-up of the Columbia River basalts around 17 Ma and later age-progressing volcanism within the Snake River Plain. Though debated, both are proposed to originate from a plume impinging on the base of the North American lithosphere [Camp and Ross, 2004]. During the Quaternary, distributed intraplate magmatism has continued although with much lower intensity than during Oligocene and Miocene.

[9] The relationship between past episodes of subduction and the presence of high seismic velocity within mantle tomography for NA have been explored by several groups, including Grand [1994] and Ren *et al.* [2007]. The ancient Farallon plate has been shown to reach the lower mantle under the Great Plains, east of our studied area. More recent tomographies, some taking advantage of the USArray data set, have shown a variety of structures interpreted as fossil subduction [Sigloch *et al.*, 2008; Burdick *et al.*, 2010; Schmandt and Humphreys, 2011], slab fragmentation [Sigloch *et al.*, 2008; Obrebski *et al.*, 2010] and lithospheric dripping [Hales *et al.*, 2005; West *et al.*, 2009; Levander *et al.*, 2011]. A plume has been proposed to exist under the Yellowstone hot spot [Schmandt *et al.*, 2012a], at the triple border between Idaho, Wyoming, and Montana (Figure 1). Interactions between a plume and the subducted Farallon plate may explain the complicated tectonic history of this region [Obrebski *et al.*, 2010].

[10] In view of the large amount of subducted material buried into the mantle, the western U.S. is of great interest for quantifying relative contributions of thermal and compositional heterogeneity to mantle discontinuity structure.

2. Data and Method

[11] P-to-S conversions (Ps) result from teleseismic P waves that convert part of their energy to shear waves at seismic boundaries under the array [e.g., Tauzin *et al.*, 2008]. Because differences between source functions for recorded seismicity can cause significant differences in the waveforms on recorded seismograms, the data must be “equalized” through the construction of receiver functions [Langston, 1979]. The resulting time series show the elastic response of the Earth beneath receivers and can be back-projected via migration [e.g., Rondenay, 2009] to image interfaces at the origin of coherent amplitudes on seismograms.

[12] In this approach, the background medium under the array is assumed to be horizontally stratified. In some cases, this approximation may be inadequate for the source estimate and the migration. Accurate source estimation as well as proper migration such as reverse time migration (RTM) of the direct and converted wavefield [e.g., Shang *et al.*, 2012] would improve 3-D media imaging. In addition, we note that the increasing computational power in the last decade has enabled to invert receiver functions directly for pseudo-3-D

Vs structure (i.e., a juxtaposition of 1-D models). Shen *et al.* [2013a, 2013b] used this approach for imaging the crust and uppermost mantle beneath the central and western U.S. RTM and direct inversion are not considered here.

2.1. Data

[13] We use three-component broadband records of passive seismicity at stations deployed during the U.S. Transportable Array experiment between January 2004 and November 2009. Waveforms are obtained from the IRIS Data Management Center (<http://www.iris.edu/>) for 932 teleseismic earthquakes, occurring at depths less than 350 km, epicentral distances between 40° and 95°, and with magnitude of at least 5.5. These earthquakes were recorded during the two first deployments of the Transportable Array covering the western half of the U.S. at 820 sites (Figure 1). Due to earthquake concentration along active plate boundaries in North West Pacific and South America (inset in Figure 1), azimuthal illumination of the structure under the array is uneven, with a preferential NW-SE sampling.

2.2. Receiver Functions

[14] Two data sets are obtained by low-pass filtering the seismograms at 0.1 and 0.2 Hz, respectively. For each data set, we build receiver functions (RFs) by deconvolving the records rotated along the longitudinal axis by the records rotated along the vertical axis. As in Tauzin *et al.* [2008, 2010], we use the iterative time domain deconvolution due to Ligorria and Ammon [1999]. The highest quality data are extracted from raw and deconvolved seismograms based on signal to noise ratio criteria. The final data set consists of ~67,000 RFs providing a good coverage in P-to-S piercing points at TZ discontinuities below western U.S. A seismic section from these RFs is shown in Figure 2a. The data are aligned on the P arrival and stacked within 0.01 s/deg intervals of P wave slowness. After the direct P arrival at 0 s, clear arrivals with similar moveout are observed around 5 s, 50 s, and 70 s. These are, respectively, direct P-to-S conversions at the Moho (Pms), the 410 (P410s), and the 660 (P660s) under the array. The later part of the signal is dominated by a strong arrival (PP) associated with the P reflection at the free surface halfway between the source and the receiver.

2.3. Synthetic Data

[15] For comparison we produce for the source-receiver pairs considered in our database synthetic seismograms (in a 1-D structure) using a reflectivity algorithm [Fuchs and Muller, 1971]. We use IASP91 [Kennett and Engdahl, 1991] as the reference velocity model and source parameters from the global CMT catalogue (<http://www.globalcmt.org/>). These synthetic seismograms are then processed in the same way as the real data set (except for data quality control). Comparison with the synthetic RF section (Figure 2b) demonstrates that main features are present in the observed data (Figure 2a). A large difference arises from the use of a two-layered crust, giving a complicated pattern of interferences within the 10–20 s range of Figure 2b. It is associated with waves reflected multiple times (reverberations) within the crust (denoted as “mult”). Another difference is the larger amplitudes of the waveforms in the synthetics, which are clear for P410s and P660s arrivals and especially

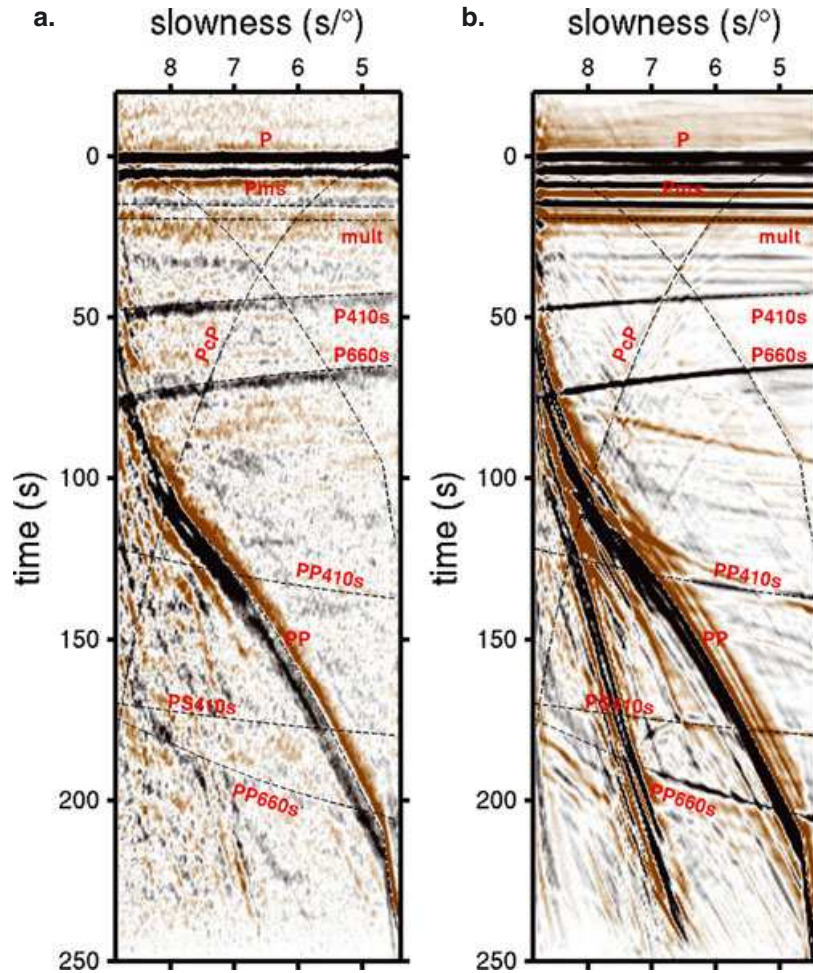


Figure 2. Time-slowness seismic sections for the $\sim 60,000$ USArray receiver functions. The use of a reversed slowness axis is similar to plot the data by increasing epicentral distances. (a) Observed and (b) synthetic data. The amplitude scale ranges between $\pm 3\%$ of the P wave amplitude for both observed and synthetic data. Data are filtered in the 5–75 s period range and aligned on the P arrival. Consecutive main seismic arrivals are indicated with their theoretical travel time curves (dashed black curves). Pms, P410s, and P660s are direct conversions at Moho, 410, and 660 discontinuities. The arrivals noted “mult” are multiple reverberations within the crust. Other reverberations (PP410s, PS410s, and PP660s) occur within layers overlying the 410 and 660 discontinuities. PP arrivals are P wave reflected below the surface halfway between sources and receivers. PcP arrivals are P reflection at the top of the core-mantle boundary.

for later arrivals (PP410s, PP660s, PP, and other multiple reflected P waves). This is the effect of various diffractions that are not accounted for by IASP91 synthetics but which reduce the summation amplitudes in the observed seismic section.

[16] Despite these differences, the comparison between real and synthetic data demonstrates the overall good quality of the U.S. Transportable Array data. In the following, we use the synthetic data to explore possible imaging artifacts due to the geographical limits of the array, the radiation patterns of seismic sources, and the effects of interfering waves such as PP at shortest distances.

2.4. CCP Stacking

[17] Our imaging procedure is based on common conversion point (CCP) stacking [e.g., Dueker and Sheehan,

1997; Zhu, 2000; Wittlinger *et al.*, 2004] and assumes locally horizontal interfaces. Rays corresponding to S legs for P-to-S conversions are back-propagated with their theoretical azimuth and incidence from each receiver to depth in the mantle. The back propagation is computed with the velocity model IASP91 [Kennett and Engdahl, 1991] after an Earth flattening transformation [Muller, 1985]. For every time sample on the RFs, the amplitude is projected to its theoretical location along the ray in the 1-D media. Combining the RF amplitude information of many rays with different directions gives the approximate locations of scatterers (or “converters”) at the origin of a coherent energy on several seismic signals. To benefit from data redundancy, stacked amplitudes within some distance of a vertical plane are then projected and averaged onto this plane to obtain 2-D depth-distance CCP sections.

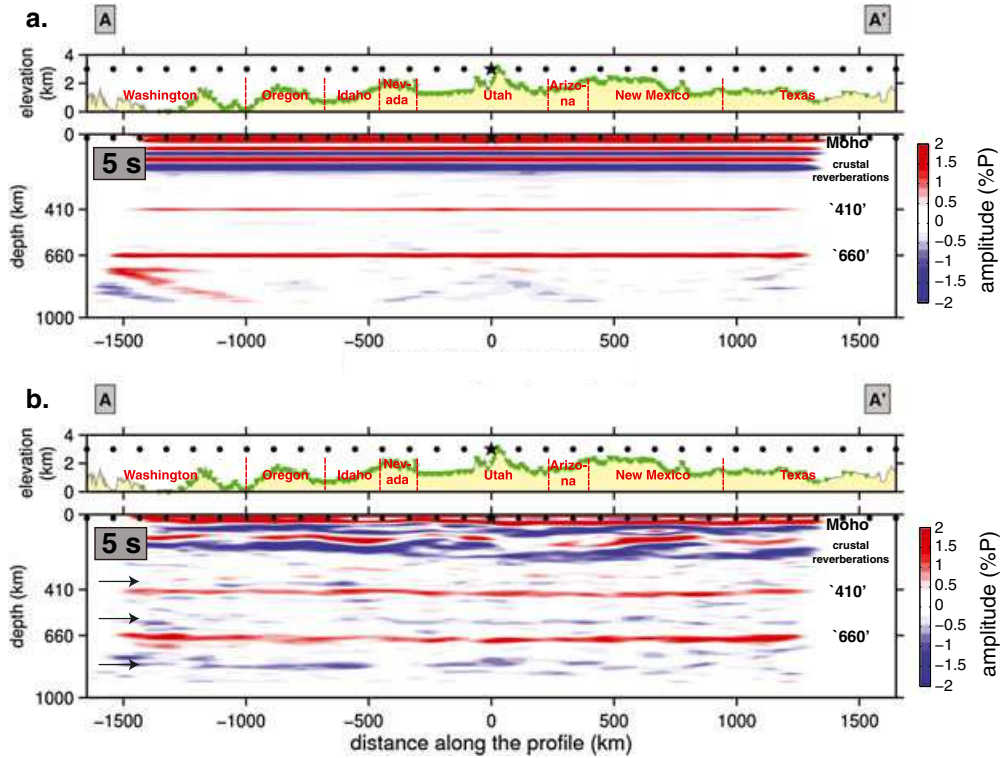


Figure 3. CCP stacked sections from USArray P-to-S receiver functions. Positive amplitudes are shown in red and negative amplitudes in blue. (a) A-A' section obtained from synthetic data computed with IASP91. The data are low-pass filtered at 5 s period. (b) Same section but for observed data. Black arrows indicate the depths of signals of specific interest.

[18] Near the edges of the imaged area, fewer data are available due to a reduced coverage in stations and/or a shorter period of recording. Because the signal-to-noise ratio is degraded when fewer data are present in the stack, CCP sections tend to be blurred in these areas. To reduce this effect, we set to zero the amplitudes within cells where the ray coverage is the poorest (<30 rays within $1 \text{ km} \times 10 \text{ km}$ cells). Finally, the CCP sections are smoothed using a gaussian weighting with the length of semi-axes corresponding to the lateral extent of the Fresnel zones of converted waves at TZ depths [Wittlinger and Farra, 2007].

[19] P-to-S conversion amplitudes are mainly determined by transmission coefficients at discontinuities and can be estimated from the P, S, and density contrasts across these discontinuities [Aki and Richards, 1980]. Over the range of incidence angles considered here, P-to-S transmission coefficients are primarily controlled by the shear wave velocity contrast, with only 10% contribution from the density contrast [Schaeffer and Bostock, 2010]. Amplitudes within CCP sections thus can be viewed as proxies for contrasts in shear wave velocity V_s . The amplitudes are positive (or negative) for an increase (or decrease) of V_s velocity with depth.

[20] The vertical resolution achieved by the data, i.e., the ability to separate vertically two converters, is given by a quarter to a half the S wavelength λ and thus depends on the frequency content of the data ($\lambda = V_s \cdot T$, T the period). With $T = 10$ and 5 s, the minimum resolvable distances between converters at TZ depths are respectively ~ 20 and ~ 10 km.

[21] The sensitivity of conversions to the sharpness of velocity gradients depends also on the frequency content

of the data [Bostock, 1999]. The difference between a step and a gradual transition becomes indistinguishable for transitions occurring across thicknesses less than one fourths of the S wavelength, but this sensitivity decreases significantly for transitions larger than half the P wavelength. A separation between V_s contrast and sharpness of gradients can be obtained from the frequency analysis of Ps amplitudes [e.g., van der Meijde et al., 2003; Schmandt et al., 2012b]. Though such a multiple frequency approach has been attempted here, a detailed analysis is beyond the scope of this paper.

3. Seismic Cross Sections

[22] In Figure 3a, we show the result of applying CCP stacking along the profile A-A' for synthetic RFs computed with IASP91. The A-A' profile (see Figure 1) extends from north-west Washington to Texas. For the first-order views of the mantle, we average all data within ± 250 km of the cross sections. Positive amplitudes are, as expected, observed for the Moho discontinuity at 35 km depth, for the 410, and for the 660 (Figure 3a). In IASP91, the TZ discontinuities are defined by steps with 4% and 6% V_s increases. Corresponding conversion amplitudes are $\sim 1.25\%$ and $\sim 2.5\%$, respectively (Figure 3a). These synthetic amplitudes result from the combined effects of the transmission of Pds waves below the stations, the projection of ground vibrations on recording components, and the weighting effects of filtering/stacking/smoothing in the CCP approach.

[23] Reverberations are waves reflected multiple times in layers overlying strong seismic discontinuities. They always

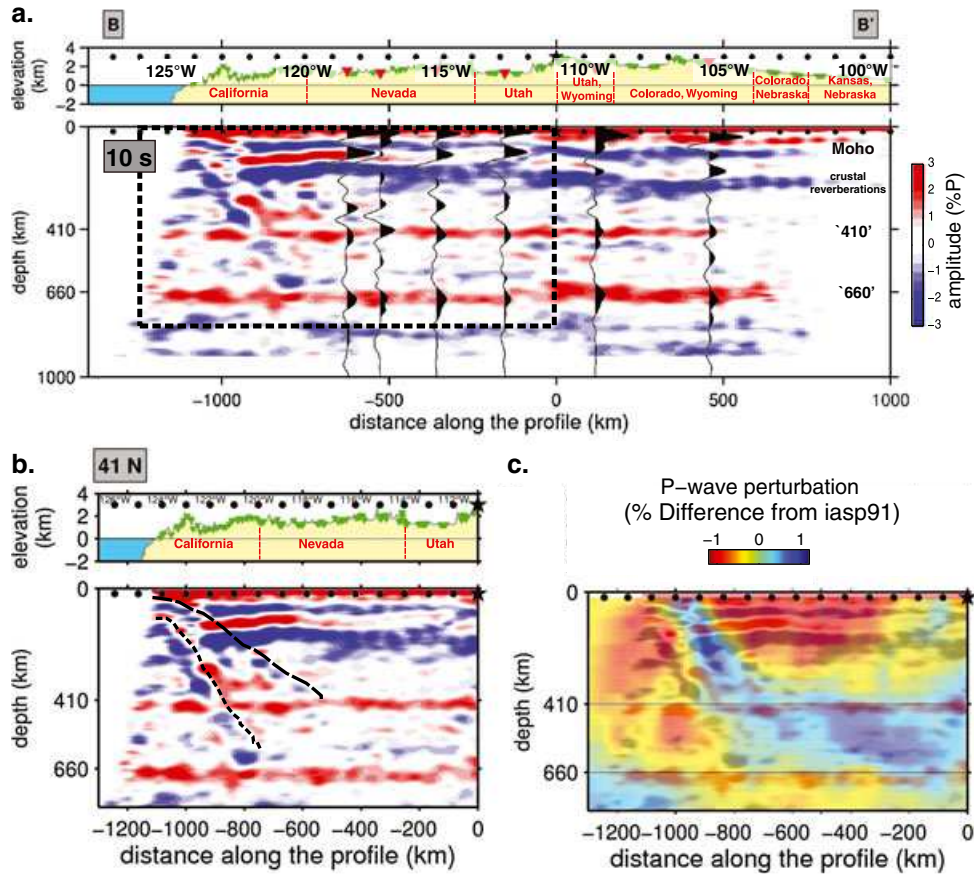


Figure 4. The Gorda-Juan de Fuca plate. (a) Observed section for the B-B' profile from low-pass-filtered data at 10 s period. The horizontal smoothing emphasizes the vertically coherent structures. Black waveforms are receiver functions from *Tauzin et al.* [2010], taken from stations within ± 250 km of the profile. They are consistent with the results of the present study. The black frame is the region of the mantle interpreted in Figures 4b and 4c. (b) Interpretation of a zoom in on the first 1300 km of the B-B' profile (black frame in a). The inferred top of the dipping structure is indicated with a long dashed line, the bottom with a short dashed line. Longitudes are indicated on top of the topographic profiles. (c) Superimposition of the conversion image with a cross section through the P wave tomographic model of *Burdick et al.* [2010].

arrive later than direct conversions and, for a sharp and strong velocity contrast, significantly obscure the signal associated with real structure. In Figure 3a, reverberations within the crust completely overwhelm the signal associated with the structure between 150 and 200 km depth.

[24] Just below the 660 discontinuity, the IASP91 model has a pronounced V_s gradient extending over 100 km. As expected, 5 s low-pass-filtered data are not able to retrieve this gradient extending over a distance larger than the P wavelength. In the lower mantle, we observe trails of amplitudes extending from the edges to the center of the profile. The primary reason for these features, for instance beneath Washington, may likely be incoherent stacking of PP arrivals for $\sim 40^\circ$ – 55° events (i.e., slowness > 8 s/deg in Figure 2b).

[25] The result of the migration of the USArray data along the A-A' profile is shown in Figure 3b. Besides the Moho conversions and the crustal reverberations, the 410 and 660 are the most prominent signals. However, various other coherent converters can be observed in the mantle below western U.S. Anomalous signals are detected atop the 410, at the bottom of the TZ, and within the uppermost

lower mantle (black arrows). Most of these signals have negative amplitudes suggesting that they are shear wave velocity reductions. These unexpected signals are absent from the synthetic data computed using IASP91 (Figure 3a).

[26] The B-B' profile is chosen at the latitude of the Mendocino fracture zone (41°N), a long-lived transform fault at the southern limit of the Gorda-Juan de Fuca plate (see Figure 1). The CCP section obtained from low-pass filtering, the data at 10 s period are shown in Figures 4a and 4b. Below northern Nevada, the 410 is significantly uplifted at $\sim 117^\circ\text{W}$ (-600 km). This 12–16 km elevation is similar to what was observed on RF data (black waveforms in Figure 4a) in the global study of *Tauzin et al.* [2010]. A structure dips eastward in the mantle below California; we note that in B-B', we use longer period data than in A-A' in order to make this structure more noticeable. Its lower part (Figure 4b), which is the most clearly defined, reaches the bottom of the TZ approximately at the border between California and Nevada ($\sim 120^\circ\text{W}$; -800 km). Its upper limit is more uncertain. It reaches the top of the TZ at $\sim 117^\circ\text{W}$ (-600 km), below northern Nevada, just west of the uplift of the 410. This structure coincides with the presence of the strongest

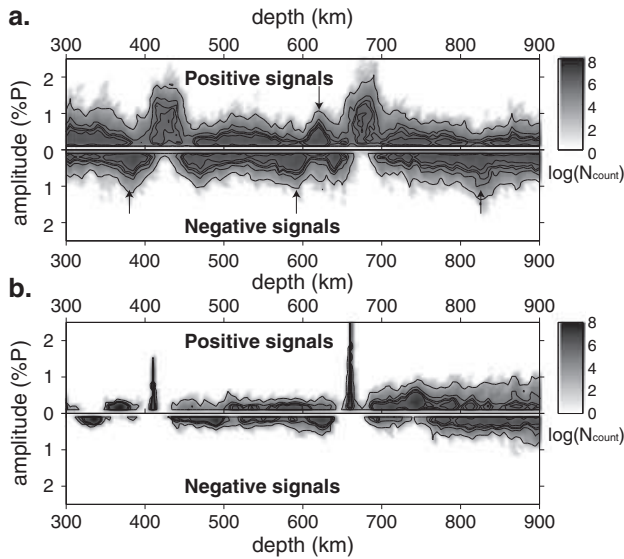


Figure 5. (a) Real and (b) synthetic depth/amplitude distributions of the maxima of signals measured from CCP stacking along profiles across western U.S. For a given couple of depth and amplitude, the logarithm of the number of signals is colored in gray. The arrows in Figure 5a indicate signals of specific interest.

negative signals atop the 410 in global RFs from *Tauzin et al.* [2010] (Figure 4a).

4. Mapping the Discontinuities

[27] With perfect sampling, the 3-D structure of mantle discontinuities can be retrieved robustly by interpolation of a set of parallel 2-D sections taken in arbitrary direction, and sections in different directions would give the same result. In practice, this is not always the case, and the degree of dissimilarity provides information about (1) the effect of imperfect illumination of the structure under the array, (2) the sensitivity to the direction of projection of RF amplitudes on the vertical plane of the profile, (3) the influence of smoothing parameters used for imagery, and (4) the potential effect of interfering phases. In order to establish the robustness of the main observations in our CCP images (Figures 3 and 4), we apply the CCP stacking along orthogonal profiles, at intervals of 0.5° both in longitude and in latitude. We note that a similar approach was used by *Cao et al.* [2011] in their SS precursor study of the transition zone discontinuities beneath Hawaii.

[28] Due to the ray geometry below the stations (a cone), the projection tends to gather information across an area that increases with depth. This may produce significant distortion in the discontinuity images. To improve the resolution with respect to Figures 3 and 4, we restrict the lateral averaging to converters within ± 100 km of the profiles.

[29] The distribution of positive and negative maxima in P-to-S converted signals along these CCP profiles is shown as a function of depth in Figure 5a. Conspicuous peaks appear at mean depths of the 410 and 660, consistent with expectations (that is, synthetics) from IASP91 (Figure 5b). We note that the synthetic amplitudes are

distributed across a much narrower range than those observed, in large part because of the varying topography of real interfaces.

[30] A few additional smaller signals arise above the noise at depths indicated by the black arrows in Figure 5a. Negative converters are confirmed at depths around 380 km and 590 km. An additional converter, not identified on the cross sections of Figure 3, may be present with positive amplitudes around 630 km depth. We do not observe a clear interface near 520 km depth contrary to the study of *Schmandt et al.* [2012b]. Mineralogical models [e.g., *Cammarano et al.*, 2005; *Ricard et al.*, 2005; *Stixrude and Lithgow-Bertelloni*, 2005] and seismology [e.g., *Shearer*, 2000] indicate that for a pyrolytic bulk mantle composition, the wadsleyite to ringwoodite transition is not associated with an important change of elastic properties (about 5 times smaller than for the 410 and the 660). The detection of a clear interface may also be difficult because of the presence of other transitions (dissolution of pyroxene into garnet slightly above and exsolution of calcium perovskite slightly deeper), of laterally varying basalt fraction [e.g., *Xu et al.*, 2008] and water content [e.g., *Jacobsen and Smyth*, 2006; *Mao et al.*, 2008]. The wadsleyite to ringwoodite transition might contribute, however, to the broad maximum observed between 510 and 550 km depth in Figure 5a and in Figure 4a.

[31] The amplitude range is the strongest in the lower mantle, both for the observations (Figure 5a) and for the synthetics (Figure 5b). PP waveforms having not been excluded, it is likely that they distort any true structures below the 660. Strong converters may exist in the lower mantle under western U.S. (Figures 3b, 4a, and 5a, in particular near 820 km depth). These features have also been reported in *Schmandt et al.* [2012a] in which RFs were muted before the PP arrival. However, we consider the uncertainties too large and do not discuss further these structures.

4.1. Picking the Main Converters

[32] Having found the depth ranges where coherent converters are the most likely to occur, we now describe their geographical distribution. In a first attempt, we pick by hand the coherent signal along individual 2-D profiles (e.g., Figure 6) and record their position, depth, and amplitude. For each interface, maps derived from the north-south and east-west cross sections are compared to check the robustness of the imaging. For the 410 and 660, the topographies based on north-south and east-west cross sections are very similar, with small differences arising mainly from the application of the smoothing in the last step of CCP imaging: anomalies are slightly elongated in the directions of the profiles.

[33] We also apply an approach that is less subjective to biases inherent to a visual picking. We proceed with a “blind” analysis of signal occurrences within our 3D amplitude block below USArray. We simply detect the maxima of signals around the 410 and 660 depths above a threshold corresponding to 0.6% the P wave amplitude. Such a threshold corresponds approximately to the minimum measured amplitude when picking the 410 signal by hand.

[34] The maps of interfaces obtained by automatic picking are significantly more speckled than those derived by handpicking on profiles, which suggests that visual pick-

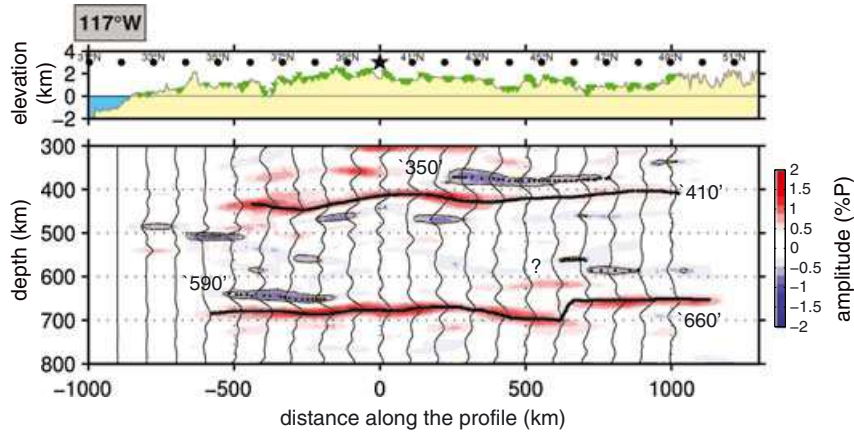


Figure 6. Example of picking P-to-S seismic signals along a 117°W profile. Waveforms in black are CCP signals extracted every 100 km along the profile. Picked conversions at the 410, at the 660, and for negative signals atop the 410 (the 350) and within the TZ (the 590) are outlined with black dots. This picking operation is applied for profiles every 0.5° in latitude and longitude. Latitudes are indicated on top of the topographic profile.

ing enhances the lateral continuity of the structures. The strongest patterns are, however, coherently retrieved by the two methods.

[35] The final maps for discontinuities (Figures 7 and 9) are then built by combining the north-south and east-west maps obtained by visual picking (i.e., union and average of the two maps).

4.2. Main Discontinuities

[36] In Figure 7, we present maps of 410 topography and TZ thickness. The 410 and 660 appear significantly deeper than in IASP91, at 424 km for the former and 676 km for the latter, giving a 252 km thick TZ. The standard deviations of distribution of measurements for the 410, the 660, and the TZ thickness are, respectively, 10 km, 9 km, and 8 km. This is consistent with previous observations by *Cao et al.* [2011] who also used IASP91 for migration.

[37] We find a strong trade-off between the depths of discontinuities and the overlying velocity structure: a lithosphere faster (or slower) than IASP91 leads to an apparent uplift (or downwarp) of the interfaces. The correlation coefficient between the 410 topography and P wave velocity anomalies above the TZ [*Burdick et al.*, 2010] is -0.67 . Although lower (-0.4), the correlation also exists for the 660.

[38] This trade-off has been discussed in detail by *Eager et al.* [2010], *Cao and Levander* [2010], and *Schmandt et al.* [2012a]. A 5% V_s change from the reference velocity model over 100 km depth would correspond to a 10–15 km apparent depth variation of an underlying discontinuity. Choosing a different reference velocity model changes the mean absolute depth of discontinuities, and taking into account 3-D lateral variations of velocities reduces significantly the standard deviations of the 410 and 660 topographies around their average depths [*Eager et al.*, 2010; *Cao and Levander*, 2010; *Schmandt et al.*, 2012a]. When no corrections for velocity are applied, it is much more reliable to consider the distances between interfaces rather than their absolute positions. *Schmandt et al.* [2012a] indeed showed for western U.S. that the 3-D velocity dependence of the TZ

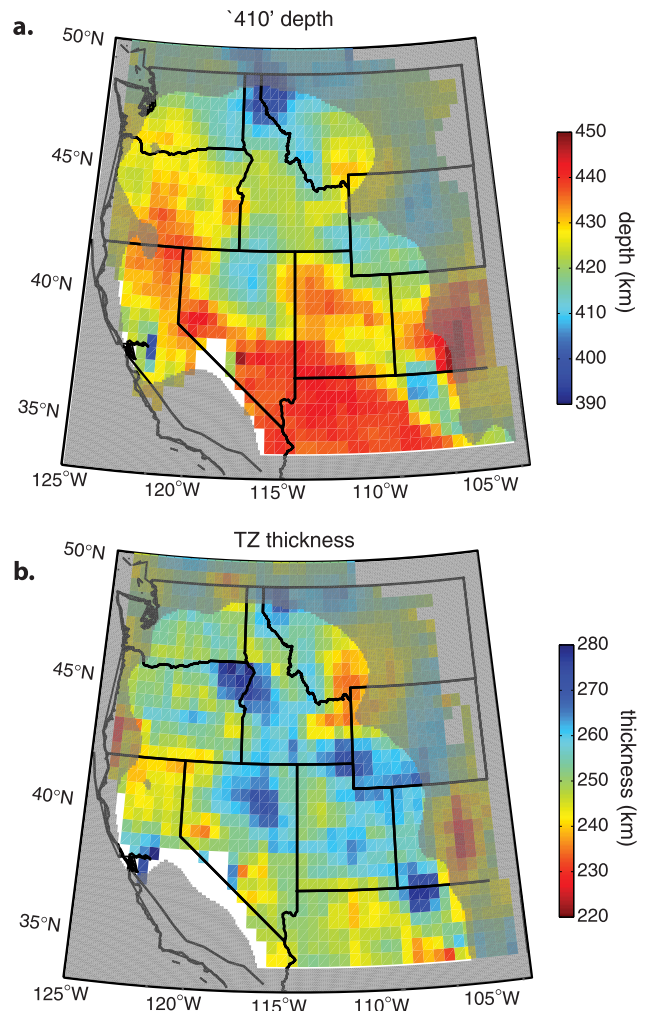


Figure 7. (a) Map of the 410 topography. (b) Map of the transition zone thickness. The mask in gray hides regions with poor data coverage.

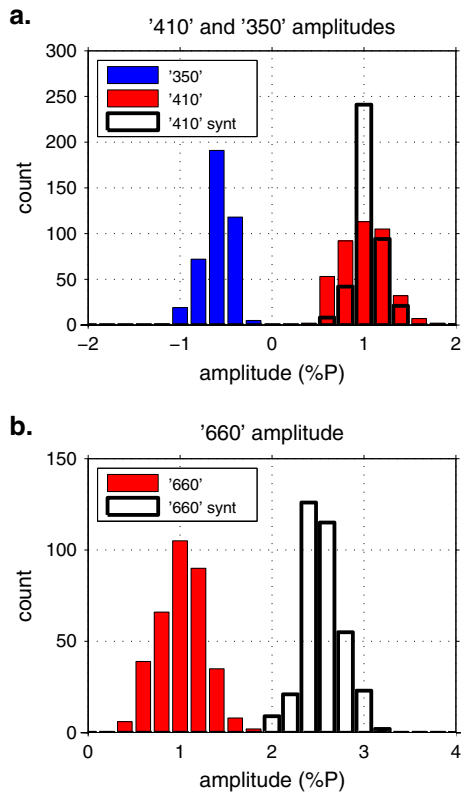


Figure 8. Histograms for P-to-S conversion amplitudes at TZ discontinuities. (a) Histograms for conversions at the 410 and 350 discontinuities. (b) Same as in Figure 8a but for the 660. Plain and empty histograms are for observed and synthetic data, respectively. Although the 410 reflectance is in agreement with IASP91, the observed 660 reflectance seems at least two times smaller than the synthetics.

thickness (Figure 7b) can be partially neglected. This is why we show in subsequent figures the depth separation between interfaces instead of their absolute depths.

[39] Figure 7b reveals that the TZ is thickened by ~ 20 km under northern Nevada and ~ 25 km under northeast Oregon. This is consistent with maps obtained from earlier studies [Eager *et al.*, 2010; Cao and Levander, 2010; Schmandt *et al.*, 2012a]. The region of the most significant TZ thinning is Yellowstone (-16 km). This also confirms the observation of Schmandt *et al.* [2012a]. Under northern Nevada, the TZ thickening is most likely related to an uplift of the 410 (Figure 7a). This uplift is visible on the B-B' profile at 117° W longitude (Figure 4b). A spurious uplift would be expected if the mantle were fast above the interface. However, tomography [e.g., Burdick *et al.*, 2010] indicates that the mantle is on average slower in this region suggesting that the actual uplift may be even larger than inferred here. Below northeast Oregon, the thickened TZ (Figure 7b) is associated with a sharp jump in the 660 apparent topography as observed at $\sim 45^\circ$ N in Figure 6. In this case, it is possible that the assumption of local “horizontal” interfaces is violated.

[40] In Figure 8, we compare the amplitudes of P-to-S conversions at TZ discontinuities to those for IASP91. The 410 amplitude is close to that of the synthetic data for most measurements across western U.S. This is not

the case for the 660. The average observed-to-synthetic amplitude ratio is $\sim 1 : 1$ for the 410 but $\sim 1 : 2$ for the 660. The IASP91 shear wave velocity contrasts at 410 and 660 are 4% and 6%, respectively, and our results suggest that the 660 discontinuity under western U.S. has a shear velocity contrast equivalent to that at 410 ($\sim 4\%$ ΔV_s). An alternative would be that the 660 transition does not occur as a discontinuity but as a gradual transition across a layer of a few P wavelengths. This view is supported by multiple-frequency analysis of stacked USArray RFs by Schmandt *et al.* [2012b].

[41] Geographical variations of conversion amplitudes are shown in Figures 9a and 9b. Low amplitudes are observed in a few locations. This cannot be related to inhomogeneities in the data coverage which is dense everywhere. For the 410 (Figure 9a), a narrow band of low amplitudes is found at the western border of Idaho, elongated in a north-south direction from 43° N to 49° N. For the 660 (Figure 9b), two regions are mapped with anomalously low amplitudes in southern Idaho and (locally) within Utah.

[42] Amplitude measurements on synthetic data indicate that artificial patterns are introduced in the recovery of synthetic conversion amplitudes (Figures 9c and 9d). Regional variations are observed with a gradual increase of conversion amplitudes from NW to SE, in particular for the 660 discontinuity. These artificial patterns may also be introduced in the observations (Figures 9a and 9b) as we found a weak positive correlation between observed conversion amplitudes and synthetic ones (0.4 for the 410; 0.2 for the 660). Moreover, no noise was added to the synthetic RFs so, although averaged out, a larger uncertainty can be expected in presence of random noise in the observed seismograms.

4.3. Minor Discontinuities

[43] We apply the same picking operation to constrain signal above the 410, that is, in the 330–400 km depth range. A negative conversion above the 410, referred to here as the 350 [Vinnik and Farra, 2007], spreads across a large part of western U.S. (Figure 10a). It confirms earlier observations from Song *et al.* [2004], Jasbinsek and Dueker [2007], and Schmandt *et al.* [2011]. The depth of the signal varies within ± 11 km from 382 km with no apparent correlation with the 410 topography.

[44] Figure 10a indicates that the depth separation between the 410 and this negative converter varies from 25 to 100 km. In the most continuous part, extending from north-east Oregon to south-west Idaho, the distance between these interfaces is about 42 km, but it varies continuously except in a narrow band at the border between Oregon and California where it reaches ~ 100 km (Figure 10a). This is also a region, however, where the ray coverage from the Transportable Array is relatively sparse. A thick layer between the 410 and the negative converter is also present in the southeast in Colorado and Kansas (60–70 km) and—locally—in eastern Oregon (50–70 km).

[45] Amplitudes of conversions at the 350 are on average half the amplitude of the P410s ($\sim 0.5\% \pm 0.15\%$ the P wave amplitude in Figure 8a). This would correspond to an $\sim 2\%$ V_s reduction, consistent with observations from Vinnik *et al.* [2010] in the area and from Tauzin *et al.* [2010] globally. We find however significant regional variations (Figure 10b) with the strongest conversions occurring

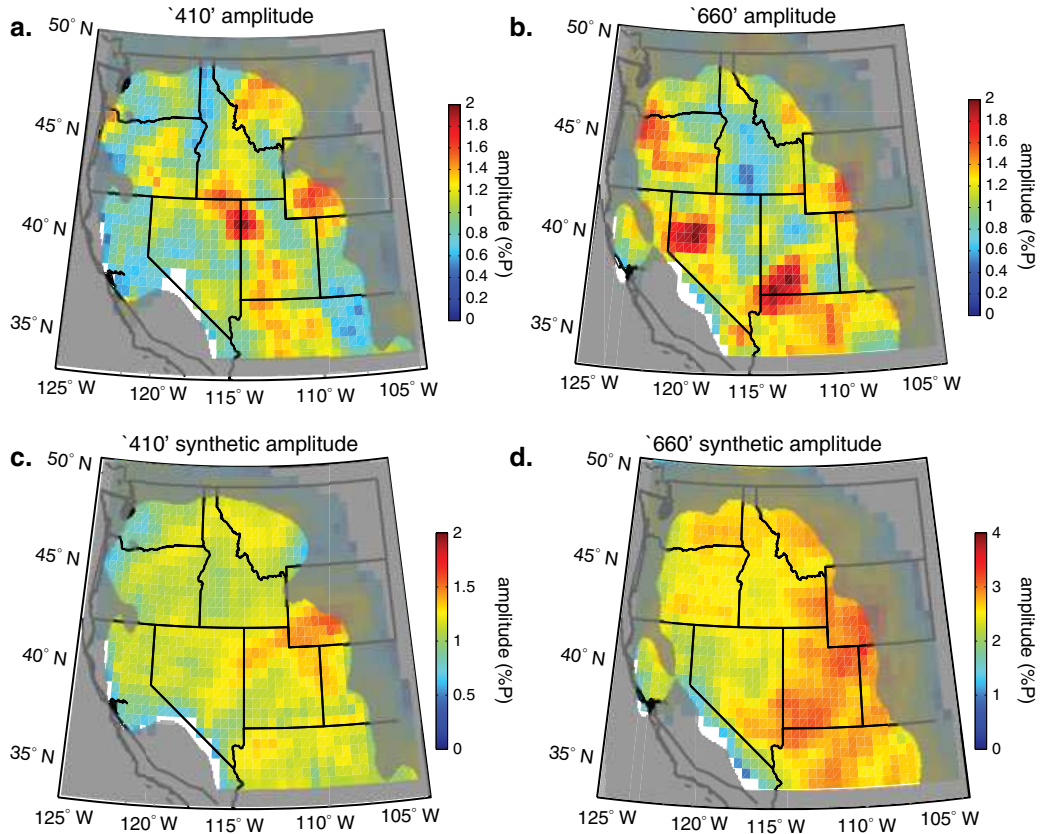


Figure 9. (a) Map of P-to-S conversion amplitudes at the 410. (b) Map of P-to-S conversion amplitudes at the 660. (c and d) Same as in Figures 9a and 9b but for synthetic data computed with IASP91. Note the difference in the color scale for the synthetic amplitudes at the 660. The mask in gray hides regions with poor data coverage.

beneath southwestern Idaho, southwest of Wyoming, and the western part of the border between Oregon and Washington. In these regions, the P350s amplitude may exceed the P410s amplitude by 20%. We note however that this is less than reported in the studies of *Jasbinsek and Dueker* [2007] and *Jasbinsek et al.* [2010].

[46] Other depth ranges showing statistically significant converters are from 540 to 630 km, with a negative signal referred to as the 590 and a positive signal between 600 and 650 km referred to as the 630. The 590 (Figure 10c) spreads over the entire western U.S. (at a depth of ~ 585 km). Its vertical separation from the 660 is on average 90 ± 20 km. It is the most continuous in the south-east of the study area. The narrowest zone (~ 40 km) is located along the western border of Nevada and corresponds to the bottom of the dipping structure observed at 41°N in Figures 4a and 4b. The 630 km signal (Figure 10d) spreads over a smaller area than the other converters. It is mostly seen beneath the triple border between Idaho, Washington, and Oregon and further west in south-west Montana. A strong increase in its distance to the 660 is observed below western Idaho. This is due to the large depression of the 660 (Figure 6) in the area.

5. Conversion Imaging and Tomography

[47] The location of the structure dipping eastward below California at $\sim 41^\circ\text{N}$ (Figure 4b) coincides with the fast velocity anomalies revealed by P wave tomography

(Figure 4c). Most tomographic studies [e.g., *Sigloch et al.*, 2008; *Burdick et al.*, 2010; *Obrebski et al.*, 2011] have related these anomalies to the Gorda plate subducting steeply below northern California. We show here that this plate has also a signature in CCP images, that is, converters with different slopes in the mantle (Figure 4b). Taking the uppermost converter as the top of a plate indicates that the slab reaches the TZ near $\sim 117^\circ\text{W}$ (~ 600 km) along the profile. It is not possible to assess the precise structure of the slab, however, as our CCP algorithm is not specifically designed for imaging dipping structures (see section 6).

[48] In Figure 11, we look at the structure of discontinuities from conversion imaging on a sequence of cross-sections from south to north. South of 38°N , we do not see evidence for the presence of a dipping structure (i.e., any of the two apparent converters), but from 40° to 44°N , a clear signature is found. Although less visible, the signature can be tracked up to 46°N where it almost disappears.

6. Discussion

6.1. Limitations

[49] With the method applied, there are several sources of possible imaging artifacts: first, the approximation of a flat layered mantle structure; second, the absence of corrections for 3D velocity variations relative to the reference model; and, third artifacts arising directly from signal processing or phase interferences.

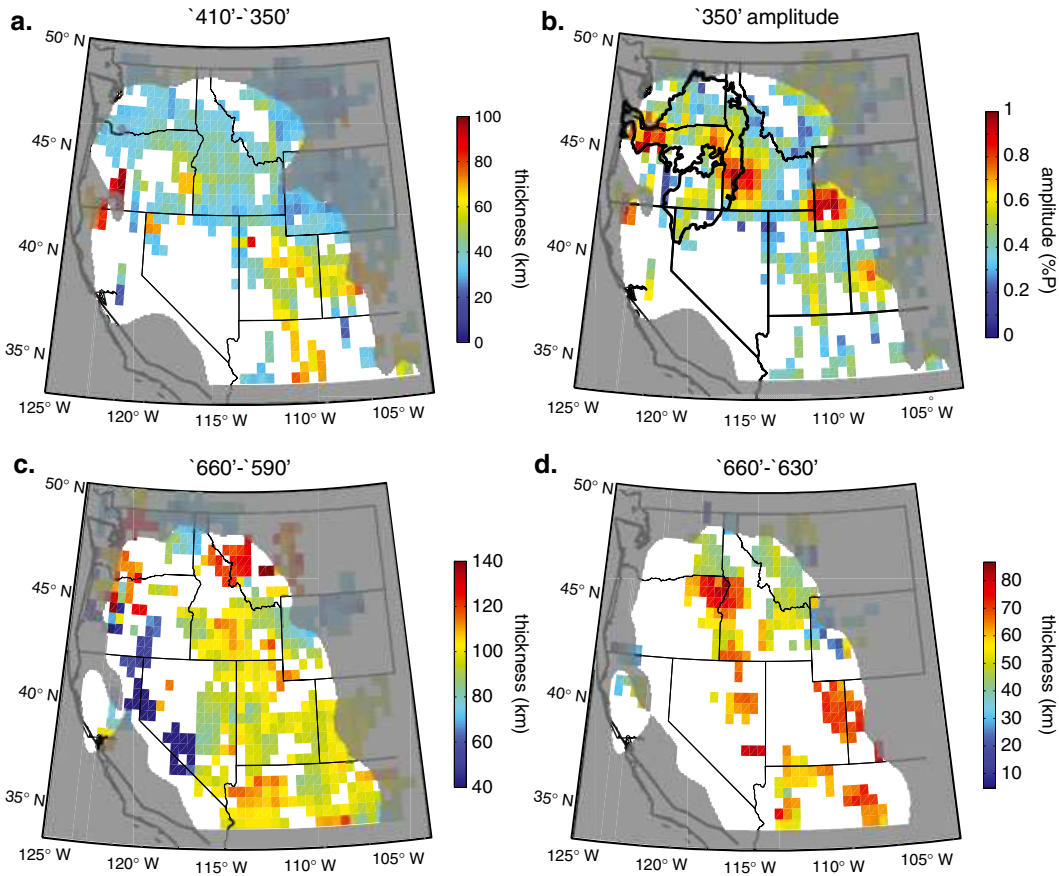


Figure 10. Layers within the TZ. (a) Thickness of the low velocity layer atop the 410. (b) Negative conversion amplitude at the top of the layer (the 350 discontinuity). The black contour from *Camp and Ross* [2004] delineates the region covered by the Columbia River flood basalts (CRB). (c) Distance between the 660 and a negative discontinuity at ~ 590 km depth. (d) Distance between the 660 and a positive discontinuity at ~ 620 km depth.

[50] First, the type of source estimate in this RF analysis assumes horizontal interfaces at depth. Indeed, the teleseismic source is here simply approximated by the vertical component record at each station. Strong multipathing of the direct P wave, for instance for rays oriented subparallel to a dipping slab, could compromise the deconvolution and introduce energy in the CCP image not located on an interface. This could be a concern for imaging the Gorda-Juan de Fuca slab, as there has been evidence for multipathing of teleseismic phases for events from eastern azimuths [*Sun and Helmberger*, 2011]. In addition, due to ray tracing within a 1-D Earth model and the assumption that Pp direct transmission and Ps conversions occur at same depths, CCP migration is designed also to be accurate only for flat structures [*Abe et al.*, 2011]. In the case of a 3-D structure, rays may deviate from their theoretical paths before reaching the surface. Using theoretical ray geometry for back-projection of the seismic signals would then lead to a blurred image of the subsurface. For instance, an isolated scatterer or sharp ends of interfaces (such as the step in the 660 in Figure 6) may produce hyperbola within CCP images [*Shang et al.*, 2012]. In addition, imaging a dipping interface may give (1) a signal with an inaccurate dip angle [e.g., *Rondenay*, 2009], (2) a complicated pattern of interference due to varying azimuth and incidence of illumination [*Frederiksen*

and *Bostock*, 2000], and (3) steeper multiple “interfaces” arising from the migration of reverberations. Given both limitations on source estimation and migration, we do not expect to resolve the detailed structure of, for instance, a subducted slab, but we expect nonetheless to detect the main signals corresponding to such a feature.

[51] Second, the main effect of uncorrected 3-D velocities will be to weaken and broaden the stacked amplitudes in CCP images. In extreme cases, delays may exceed the vertical time resolution of RF data and give multimodal peaks. *Schmandt et al.* [2012a] showed however that velocity variations below western U.S. are likely too subtle to have a major effect on the coherency of stacked P410s and P660s waveforms in CCP volumes.

[52] Third, spurious artifacts on migrated sections may result from (1) uncorrelated noise on raw and deconvolved seismograms, (2) sidelobes due to deconvolution, (3) interference of seismic phases such as PP or PcP, (4) inaccurate back-projection, and (5) multiple reverberations within the uppermost mantle structure. With the high density USArray data, uncorrelated noise is not expected to give coherent signals on RF sections. Sidelobes may be introduced by the deconvolution [*Ligorria and Ammon*, 1999] but are expected to be symmetric and on both sides of the main structural discontinuities. These features appear neither on real nor on

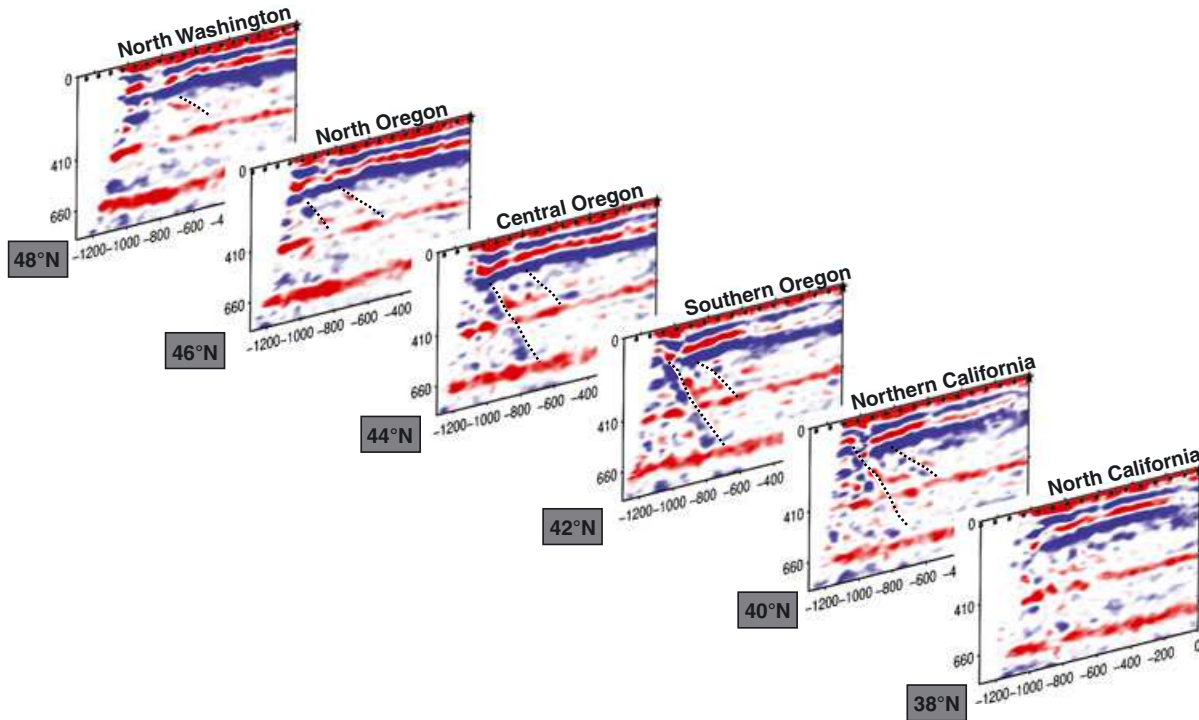


Figure 11. The Juan de Fuca and Gorda plate subduction system: interpreted CCP profiles from 38°N to 48°N latitude.

synthetic data. Interference of seismic phases such as PP and PcP may have some influence on the recovery of CCP stacked amplitudes as shown for the 410 and 660 on synthetic data (Figures 9c and 9d). However, it is unlikely that they would control the appearance of coherent converters at the scale of western U.S. as imaged in this study. Reverberations in shallow structure may be mistaken for direct conversions and wrongly interpreted as a true structure. To obtain flat “converters” in the TZ at such a large scale is, however, unlikely. In CCP images, the apparent topography of reverberations is a multiple of the original discontinuity. For example, the peak to peak topography of the Moho along the A-A’ profile (Figure 3b) is only ~ 20 km with 6 km standard deviation, whereas the first positive multiple PpPs (that has traveled 3 times the distance of the original signal) has ~ 60 km peak-to-peak topography with 18 km standard deviation. To produce a large-scale signal from reverberation in the depth ranges shown in Figure 10 would require flat and strong interfaces at shallow depths, which is unlikely.

[53] Various tests strengthened our confidence in the robustness of our results. First, by calibrating our methodology on synthetic data, we were able to retrieve the IASP91 velocity structure. Second, CCP imaging gave consistent maps along perpendicular directions. Third, two different approaches (automatic and manual picking) gave consistent results for the depths and conversion amplitudes of both major and minor seismic discontinuities. Where they overlap, our results are also in agreement with earlier studies [Eager et al., 2010; Cao and Levander, 2010; Schmandt et al., 2012a; Tauzin et al., 2010]. This is the case for the average depths of the major discontinuities, the thickness of the TZ, and the presence of additional seismic signals. The signature of the Gorda slab, consistent with independent

tomographic imaging, is also a confirmation of the reliability of our results.

6.2. Temperature Variations in the TZ

[54] Knowledge of Clapeyron slopes for olivine transformations allows us to use the seismological observations as a thermometer. The Clapeyron slope for the olivine-wadsleyite transformation at 410 km depth has been found experimentally to be between +1.5 MPa/K and +4 MPa/K [Akaogi et al., 1989; Katsura et al., 2004]. Reports for the endothermic postspinel reaction at 660 km depth are more scattered with values ranging from -0.5 MPa/K to -4 MPa/K [Litasov et al., 2005b; Ito et al., 1990]. In so far they are caused by transitions in the olivine system, topographies of discontinuities are expected to be anticorrelated. A +100 K thermal anomaly would produce a 4–10 km deepening of the 410, a 1–9 km elevation of the 660 and, as a consequence, a 5–20 km thinning of the TZ.

[55] If we ignore effects of composition, the observed variations in the topography of discontinuities and in TZ thickness imply temperature variations ranging from -400 K to +300 K below western U.S. [Eager et al., 2010; Cao and Levander, 2010; Schmandt et al., 2012a]. The coldest TZ regions occur below northern Nevada and Idaho [Eager et al., 2010; Cao and Levander, 2010; Schmandt et al., 2012a], whereas the hottest areas are associated with the Yellowstone region [Schmandt et al., 2012a].

[56] The thermal variations inferred from our measurements are consistent with what can be expected for a subduction setting and a hot spot. The uplift of the 410 and the 20 km thickening of the TZ under northern Nevada are compatible with a -100 K to -360 K thermal anomaly within the TZ. At the triple border between Oregon, Washington,

and Idaho, the 25 km increase in thickness corresponds to a -120 K to -450 K thermal cooling. Finally, in the Yellowstone region, the 16 km TZ thinning indicates a $+80$ K to $+300$ K hot anomaly.

[57] These observations suggest the presence of deep cold slab remnants below northern Nevada and north-east Oregon and a moderately hot plume within the TZ below Yellowstone.

6.3. Composition of the TZ

[58] The depth, strength, and sharpness of seismically inferred interfaces depend upon temperature and mantle composition. The pyrolite model, comprising $\sim 60\%$ olivine and 40% pyroxene and garnet, is often taken as reference for the average mantle composition. In addition to the jump due to the transformation of ringwoodite near 660 km, the garnets transform gradually to Mg and Ca-perovskite from 550 to 720 km depths [Ricard et al., 2005]. The total velocity increase results from the combination of a sharp postspinel transition and a broader phase transition in the garnet system [Weidner and Wang, 2000]. Within the range of uncertainties for mineral thermoelastic data, Cammarano et al. [2005] searched for pyrolitic models that can match seismological observations. They found olivine in pyrolite models to produce a smaller jump at the 660 compared to IASP91. This would be consistent with our finding of reduced P660s amplitudes indicating a 4% V_s contrast at the 660.

[59] The 660 transition in pyrolite has a complicated behavior with temperature. The sharp postspinel transition is endothermic while the extended transition from garnet is exothermic [Weidner and Wang, 2000]. Their opposite Clapeyron slopes may obscure the relation between the position of the seismic converters and the temperature [Hirose, 2002]. Post-garnet transitions have been invoked to explain the absence of TZ thinning under some hot spots [Deuss, 2007; Tauzin et al., 2008; Houser and Williams, 2010; Cao et al., 2011]. Under Yellowstone at least, the TZ thinning corresponds to what can be expected for a hot plume in an olivine system. In a cold area, a loop of ilmenite might be present between the garnet and the postspinel phases [Vacher et al., 1998; Hirose, 2002]. This new phase could explain the multiple positive seismic discontinuities reported beneath southern California [Simmons and Gurrola, 2000]. Interestingly, we observe the strongest 630 converter where we find the thickest and probably the coolest TZ in a narrow patch west of Idaho (see Figures 6 and 10d). Tentatively, the 630 converter could therefore mark the onset of the stability field of ilmenite.

[60] In the northern half of Idaho, a large high velocity “curtain” [Schmandt and Humphreys, 2011] extends vertically to maximum depths between 230 and 600 km. Under the triple border between Oregon, Washington, and Idaho ($\sim 117^\circ$ W) it reaches ~ 400 km depth [Roth et al., 2008; Burdick et al., 2010]. This anomaly could be a remnant of the Siletzia oceanic microplate, accreted ~ 55 Myr ago and stuck in the mantle since the subduction shifted further west to produce the Cascadia mountain ranges [Schmandt and Humphreys, 2011; Gao et al., 2011]. Our observation in the same area of a narrow band of reduced amplitudes of conversion at the 410 (see Figure 9a) would be consistent with the presence of this remnant slab. Indeed, the presence of water, which is expected to thicken and reduce the velocity jump

at the 410 [Wood, 1995], might explain our observations. Several reports [e.g., Song et al., 2004; Cao and Levander, 2010; Schmandt et al., 2011, 2012a] have indicated that the TZ could be significantly hydrated under North America.

[61] In a uniform (dry) mantle, phase transitions from low to high pressure are usually accompanied by an increase in shear velocity. The 410 and the 660 seismic signals are canonical examples of this expected behavior. Conversely, a decrease in velocity with increasing pressure cannot be readily explained by phase transitions but can be caused by the presence of volatiles or melt gravitationally stable in the mantle [e.g., Bercovici and Karato, 2003]. In western U.S., the negative 350 has been attributed to conversions atop such a melt layer [Song et al., 2004; Jasbinsek and Dueker, 2007; Jasbinsek et al., 2010; Schmandt et al., 2011]. Song et al. [2004] reported 20 to 90 km thickness variations of the layer over hundred of kilometer distances. Our 350 map reveals less dramatic variations except very locally at the border between Oregon and California. It is possible that they are due to entrainment and disruption by the regional convective flow as suggested by Schmandt et al. [2011]. The Juan de Fuca plate observed along the western margin of U.S. would somewhat support this hypothesis.

[62] Shen et al. [2008] and Shen and Blum [2003] attribute negative velocity discontinuities at 590–600 km depth and a low 660 velocity contrast beneath China and southern Africa to the former presence of subducted oceanic crust in the TZ because (i) majorite garnet, the stable assemblage within subducted oceanic crust at TZ depths, has lower seismic velocities than the average mantle [e.g., Stixrude and Lithgow-Bertelloni, 2007] and (ii) the basaltic oceanic crust may peel off from slabs in the TZ [van Keken et al., 1996]. This would lead to a stratified TZ with an anomalous seismic discontinuity structure. The geodynamical context of western U.S. with a ~ 150 Myr long subduction history could provide a similar context for setting up a basal stratification in the TZ. An alternative explanation for the low velocity layers concerns the effect of hot thermal plumes. Based on their observations, Vinnik and Farra [2007] and Vinnik et al. [2010] proposed that the layer atop the 410 is associated with the ~ 15 Myr old Columbia River flood basalts (CRB) and a related mantle plume impinging at the base of the North American lithosphere. In our study, the geography of the layer in the northwestern part of western U.S. indeed correlates with the CRB location (see Figure 10b) from Camp and Ross [2004]. However, the layer extends also far inland up to the Great Plains.

6.4. The Gorda-Juan de Fuca Plate Subduction System

[63] The main source of thermal and compositional heterogeneity in the TZ below western U.S. seems to be the ancient Farallon slab and the more recent Gorda-Juan de Fuca plate subduction system. Cao and Levander [2010], Eager et al. [2010], and Schmandt et al. [2012a] have related the uplift of the 410 below northern Nevada to the modern Juan de Fuca subduction system and the Gorda plate fragment located further west. Most tomographic models indeed show the presence of fast material dipping eastward beneath northern California and stagnant within the TZ below Nevada [e.g., Sigloch et al., 2008; Burdick et al., 2010; Obrebski et al., 2011]. This cold material should induce the uplift of the 410 exothermic transition. However,

none of the previous receiver function studies [Eager *et al.*, 2010; Cao and Levander, 2010; Schmandt *et al.*, 2012a] reported the signature of the Gorda plate in their conversion images. The only observation concerned anomalous 410 and 660 signals below northern California [Eager *et al.*, 2010].

[64] Even though dipping interfaces cannot be imaged properly with CCP stacking, along the B-B' profile (Figure 4b) and along a sequence of longitudinal profiles across western U.S. (Figure 11), we see the signature of the subducted plate. The uppermost negative “converter” reaches the TZ at $\sim 117^\circ\text{W}$ (~ 600 km) along the profiles and could be associated with the top of the Juan de Fuca plate. The strong steeper negative “converter,” reaching the base of the TZ at $\sim 120^\circ\text{W}$ (~ 800 km) and narrowly focused at the western border of Nevada, is somewhat puzzling. It could be associated with the velocity reduction at the contact of the cold plate with the underlying hotter mantle, although some reverberation artifacts from the top of the plate might be present.

[65] Our approach, stacking and projecting data from slices across the imaged volume [Wittlinger *et al.*, 2004; Nabelek *et al.*, 2009], likely makes a better use of the data redundancy than traditional RF analysis. This may explain why previous RF studies with similar data did not detect the Juan de Fuca slab.

[66] Tomographic constraints on the Juan de Fuca slab geometry include (1) a slab window [Zandt and Humphreys, 2008] roughly south of 39°N due to the northern motion of the San Andreas fault, (2) a slab anomaly (the Gorda plate at $<42^\circ\text{N}$) steeply dipping under northern California, (3) a possible absence of slab beneath central Oregon (43°N – 46°N), and (4) a fast anomaly below Washington associated with the northern portion of the Juan de Fuca plate. Our results confirm that the mantle at the southern edge of the Gorda-Juan de Fuca plate is free of slab but we see no slab disruption beneath central Oregon. More investigation would be required to understand the absence of slab in tomography beneath central Oregon [Roth *et al.*, 2008; Burdick *et al.*, 2010].

[67] Using a more sophisticated imaging technique than CCP stacking, Pavlis [2011] recovered the signature of the Farallon plate. He contoured the top of a slab gently dipping and reaching the TZ between 111°W and 108°W longitudes. We get somewhat contradictory results as our images between 40°N and 42°N indicate that the top of the slab reaches the TZ more to the west, near $\sim 117^\circ\text{W}$. Although our method is not designed to image dipping structures, the striking similarity between our images and the tomography seems to reinforce our findings. This intriguing dipping structure must be investigated further, with methods that do not rely on assumption about 1-D geometry, such as converted wave imaging based on reverse time migration [Shang *et al.*, 2012].

7. Conclusions

[68] Seismologists searching for deep mantle discontinuities usually focus on velocity increases. This is motivated by the idea that mineral pressure-induced transformations toward higher velocity phases are the unique origin of (or primary contributor to) the main structural boundaries in the mantle. Our study suggests, however, that velocity

reductions are common in the mantle, with strong signatures in conversion/reflection seismic images and suggesting effects of composition.

[69] Beneath Idaho, the TZ structure is anomalous with a sharp lateral changes in 660 depth, a thick TZ, a reduced V_s contrast at the 410, and a positive interface at ~ 630 km depth. The increased TZ thickness and the 630 discontinuity both suggest low temperatures and possibly stable ilmenite in the TZ. Water in the TZ can also reduce locally the 410 V_s contrast. The presence of a remnant of the Farallon plate, anchored in the mantle below Idaho, is a possible explanation for low temperatures and TZ hydration.

[70] At the same location, a layer with $\sim 4\%$ shear wave speed reduction and ~ 70 km thickness is present atop the 410 discontinuity. In addition, an almost continuous interface, marking shear wave velocity reductions, spreads at 590 km depth roughly from southern Idaho to the south-east of the studied area. The transition zone water filter model is a plausible model to explain a melt layer atop the 410 considering the likely hydration of the TZ below western U.S. However, it does not explain a widespread negative 590 discontinuity within the TZ.

[71] Definitive answers on the nature of the 350 and low-velocity layers in the TZ still need to be found. Western U.S. regional mantle dynamics suggests that the sharp reductions of velocities are related to subduction processes and compositional heterogeneities. It is not possible however to exclude a relationship with surface volcanism, notably with the large igneous province of the Columbia River.

[72] **Acknowledgments.** We thank Jeannot Trampert for discussions and suggestions to improve the method and the manuscript. This work was supported during a post-doctorate at Utrecht University by the Dutch National Science Foundation under Rob van der Hilst’s VICI grant NWO:VICI865.03.007. Computational resources were provided by the Netherlands Research Center for Integrated Solid Earth Science (ISES 3.2.5 High End Scientific Computation Resources). We thank the IRIS data center for providing seismological data. We also thank Victor Camp for providing a graphic contour of the Columbia River flood basalts. Discussions with Hanneke Paulssen, Nicolas Coltice, and Hervé Leloup have been helpful in improving the manuscript. We thank B. Schmandt and an anonymous reviewer for their constructive reviews.

References

- Abe, Y., T. Ohkura, K. Hirahara, and T. Shibutani (2011), Common-conversion-point stacking of receiver functions for estimating the geometry of dipping interfaces, *Geophys. J. Int.*, *3*, 1305–1311.
- Akaogi, M., E. Ito, and A. Navrotsky (1989), Olivine-modified spinel-spinel transitions in the system Mg_2SiO_4 - Fe_2SiO_4 : Calorimetric measurements, thermochemical calculation, and geophysical application, *J. Geophys. Res.*, *94*, 15,671–15,685.
- Aki, K., and P. Richards (1980), *Quantitative Seismology*, W. H. Freeman, San Francisco, Calif.
- Anderson, D. L., and K. A. Schramm (2005), Global hotspot maps, in *Plates, Plumes and Paradigms*, Geological Society of America Special Paper 388, edited by G. R. Foulger, J. H. Natland, D. C. Presnall, and D. L. Anderson, pp. 19–29, doi:10.1130/2005.2388(03).
- Bercovici, D., and S. Karato (2003), Whole mantle convection and transition-zone water filter, *Nature*, *425*, 39–44.
- Bostock, M. (1999), Seismic waves converted from velocity gradient anomalies in the Earth’s upper mantle, *Geophys. J. Int.*, *138*, 747–756.
- Burdick, S., et al. (2010), Model update January 2010: Upper mantle heterogeneity beneath North America from traveltimes tomography with global and USArray Transportable Array data, *Seismol. Res. Lett.*, *81*, 689–693.
- Cammarano, F., S. Goes, and D. Giardini (2005), One-dimensional physical reference models for the upper mantle and transition zone: Combining seismic and mineral physics constraints, *J. Geophys. Res.*, *110*, 1–17.
- Camp, V., and M. Ross (2004), Mantle dynamics and genesis of mafic magmatism in the intermontane Pacific Northwest, *J. Geophys. Res.*, *109*, 1–14, doi:10.1029/2003JB002838.

- Cao, A., and A. Levander (2010), High resolution transition zone structures of the Gorda Slab beneath the western United States: Implication for deep water subduction, *J. Geophys. Res.*, *115*, 1–13, doi:10.1029/2009JB006876.
- Cao, Q., R. van der Hilst, M. de Hoop, and S. Shim (2011), Seismic imaging of transition zone discontinuities suggests hot mantle west of Hawaii, *Science*, *332*, 1068–1071.
- Courtier, A., and J. Revenaugh (2007), Deep upper mantle melting beneath the Tasman and the Coral seas detected with multiple ScS reverberations, *Earth Planet. Sci. Lett.*, *259*, 66–76.
- Deuss, A. (2007), Seismic observations of transition zone discontinuities beneath hotspot locations, in *Plates, Plumes, and Planetary Processes*, Geological Society of America Special Paper 430, edited by G. R. Foulger and D. M. Jurdy, pp. 121–136, doi:10.1130/2007.2430(07).
- Dueker, K., and A. Sheehan (1997), Mantle discontinuity structure from mid-point stacks of converted P to S waves across the Yellowstone Hotspot Track, *J. Geophys. Res.*, *102*, 8313–8327.
- Eager, K., M. Fouch, and D. James (2010), Receiver function imaging of upper mantle complexity beneath the Pacific Northwest, United States, *Earth Planet. Sci. Lett.*, *297*, 140–152.
- Fee, D., and K. Dueker (2004), Mantle transition zone topography and structure beneath the Yellowstone hotspot, *Geophys. Res. Lett.*, *31*, 1–4.
- Frederiksen, A., and M. Bostock (2000), Modelling teleseismic waves in dipping anisotropic structures, *Geophys. J. Int.*, *141*, 401–412.
- Fuchs, K., and G. Muller (1971), Computation of synthetic seismograms with the reflectivity method and comparison with observations, *Geophys. J. R. Astron. Soc.*, *23*, 417–433.
- Gao, S., P. Silver, K. Liu, and the Kapvaal Seismic Group (2011), Crust and lithosphere structure of the northwestern U.S. with ambient noise tomography: Terrane accretion and Cascade arc development, *Earth Planet. Sci. Lett.*, *304*, 202–211.
- Grand, S. (1994), Mantle shear structure beneath the Americas and surrounding oceans, *J. Geophys. Res.*, *99*, 11,591–11,621.
- Hales, T., D. Abt, E. Humphreys, and J. Roering (2005), A lithospheric instability origin for Columbia River flood basalts and Wallowa Mountains uplift in northeast Oregon, *Nature*, *438*, 842–845.
- Helffrich, G. (2000), Topography of the transition zone seismic discontinuities, *Rev. Geophys.*, *38*, 141–158.
- Higo, Y., T. Inoue, and T. Irifune (2001), Effect of water on the spinel-postspinel transformation in Mg₂SiO₄, *Geophys. Res. Lett.*, *28*, 3505–3508.
- Hirose, K. (2002), Phase transitions in pyrolitic mantle around 670-km depth: Implications for upwelling of plumes from the lower mantle, *J. Geophys. Res.*, *107*, 1–11.
- Houser, C., and Q. Williams (2010), Reconciling Pacific 410 and 660 km discontinuity topography, transition zone shear velocity patterns, and mantle phase transitions, *Earth Planet. Sci. Lett.*, *296*, 255–266.
- Humphreys, E. (1995), Post-Laramide removal of the Farallon slab, western United States, *Geology*, *23*, 987–990.
- Irifune, T., and A. Ringwood (1993), Phase transformations in subducted oceanic crust and buoyancy relationships at depths of 600–800 km in the mantle, *Earth Planet. Sci. Lett.*, *117*, 101–110.
- Irifune, T., N. Kubo, M. Isshiki, and Y. Yamasaki (1998), Phase transformations in serpentine and transportation of water into the lower mantle, *Geophys. Res. Lett.*, *25*, 203–206.
- Ita, J., and L. Stixrude (1992), Petrology, elasticity, and composition of the mantle transition zone, *J. Geophys. Res.*, *97*, 6849–6866.
- Ito, E., M. Akaogi, L. Topor, and A. Navrotsky (1990), Negative pressure-temperature slopes for reactions forming MgSiO₃ perovskite from calorimetry, *Science*, *249*, 1275.
- Jacobsen, S., and J. Smyth (2006), Effect of water on the sound velocities of ringwoodite in the transition zone, in *Earth's Deep Water Cycle*, vol. 168, edited by S. Jacobsen and S. van der Lee, pp. 131–145, AGU monograph, AGU, Washington, D. C.
- Jasbinsek, J., and K. Dueker (2007), Ubiquitous low-velocity layer atop the 410-km discontinuity in the northern Rocky Mountains, *Geochem. Geophys. Geosyst.*, *8*, 1–19, doi:10.1029/2007GC001661.
- Jasbinsek, J., K. Dueker, and S. Hansen (2010), Characterizing the 410 km discontinuity low-velocity layer beneath the LA RISTRA array in the North American South-West, *Geochem. Geophys. Geosyst.*, *11*, 1–17.
- Katsura, T., et al. (2004), Olivine-wadsleyite transition in the system (Mg,Fe)₂SiO₄, *J. Geophys. Res.*, *109*, 1–12, doi:10.1029/2003JB002438.
- Kawamoto, T., R. Hervig, and J. Holloway (1996), Experimental evidence for a hydrous transition zone in the early Earth's mantle, *Earth Planet. Sci. Lett.*, *142*, 587–592.
- Kennett, B., and E. Engdahl (1991), Travel times for global earthquake location and phase identification, *Geophys. J. Int.*, *105*, 429–465.
- Langston, C. (1979), Structure under mont Rainier, Washington, inferred from teleseismic body waves, *J. Geophys. Res.*, *84*, 4749–4762.
- Levander, A., B. Schmandt, M. Miller, K. Liu, K. Karlstrom, R. Crow, C.-T. Lee, and E. Humphreys (2011), Continuing Colorado plateau uplift by delamination style convective lithospheric downwelling, *Nature*, *472*, 461–466.
- Ligorria, J., and C. Ammon (1999), Iterative deconvolution and receiver-function estimation, *Bull. Seismol. Soc. Am.*, *85*, 1395–1400.
- Litasov, K., E. Ohtani, A. Sano, and A. Suzuki (2005a), Wet subduction versus cold subduction, *Geophys. Res. Lett.*, *32*, 1–5.
- Litasov, K., E. Ohtani, A. Sano, A. Suzuki, and A. Funakoshi (2005b), In situ x-ray diffraction study of post-spinel transformation in a peridotite mantle: Implication for the 660-km discontinuity, *Earth Planet. Sci. Lett.*, *238*, 311–328.
- Lithgow-Bertelloni, C., and M. Richards (1998), The dynamics of Cenozoic and Mesozoic plate motions, *Rev. Geophys.*, *36*, 2–78.
- Mao, Z., S. Jacobsen, F. Jiang, J. Smyth, C. Holl, and T. Duffy (2008), Elasticity of hydrous wadsleyite to 12 GPa: Implications for Earth's transition zone, *Geophys. Res. Lett.*, *35*, 1–5.
- Muller, G. (1985), The reflectivity method: A tutorial, *J. Geophys.*, *58*, 153–174.
- Nabelek, J., et al. (2009), Underplating in the Himalaya-Tibet collision zone revealed by the Hi-CLIMB experiment, *Science*, *325*, 1371–1374.
- Obrebski, M., R. Allen, M. Xue, and S. Hung (2010), Slab-plume interaction beneath the Pacific Northwest, *Geophys. Res. Lett.*, *37*, 1–6.
- Obrebski, M., R. Allen, F. Pollitz, and S. Hung (2011), Lithosphere-asthenosphere interaction beneath the western United States from the joint inversion of body-wave traveltimes and surface-wave phase velocities, *Geophys. J. Int.*, *185*, 1003–1021.
- Pavlis, G. (2011), Three-dimensional wavefield imaging of data from the USArray: New constraints on the geometry of the Farallon slab, *Geosphere*, *7*, 785–801.
- Ren, Y., E. Stutzmann, R. van der Hilst, and J. Besse (2007), Understanding seismic heterogeneities in the lower mantle beneath the Americas from seismic tomography and plate tectonic history, *J. Geophys. Res.*, *112*, 1–15.
- Revenaugh, J., and S. Sipkin (1994), Seismic evidence for silicate melt atop the 410-km mantle discontinuity, *Nature*, *369*, 474–476.
- Ricard, Y., E. Mattern, and J. Matas (2005), Synthetic tomographic images of slabs from mineral physics, in *Earth's Deep Interior: Structure, Composition, and Evolution*, vol. 160, edited by R. van der Hilst, J. Bass, J. Matas, and J. Trampert, pp. 283–300, American Geophysical Union, Washington, D.C.
- Rondenay, S. (2009), Upper mantle imaging with array recordings of converted and scattered teleseismic waves, *Surv. Geophys.*, *30*, 377–405.
- Roth, S., M. Fouch, D. James, and R. Carlson (2008), Three-dimensional seismic velocity structure of the northwestern United States, *Geophys. Res. Lett.*, *35*, 1–6.
- Schaeffer, A., and M. Bostock (2010), A low velocity zone atop the transition zone in northwestern Canada, *J. Geophys. Res.*, *115*, 1–22, doi:10.1029/2009JB006856.
- Schmandt, B., and E. Humphreys (2011), Seismically imaged relict slab from the 55 Ma Siletzia accretion to the northwest United States, *Geology*, *39*, 175–178.
- Schmandt, B., K. Dueker, S. Hansen, J. Jasbinsek, and Z. Zhang (2011), A sporadic low-velocity layer atop the western U.S. mantle transition zone and short-wavelength variations in transition zone discontinuities, *Geochem. Geophys. Geosyst.*, *12*, 1–26.
- Schmandt, B., K. Dueker, E. Humphreys, and S. Hansen (2012a), Hot mantle upwelling across the 660 beneath Yellowstone, *Earth Planet. Sci. Lett.*, *331–332*, 224–236.
- Schmandt, B., K. Dueker, E. Humphreys, and S. Hansen (2012b), Mantle transition zone shear velocity gradients beneath USArray, *Earth Planet. Sci. Lett.*, *355–356*, 119–130.
- Shang, X., M. de Hoop, and R. van der Hilst (2012), Beyond receiver functions: Passive source reverse time migration and inverse scattering of converted waves, *Geophys. Res. Lett.*, *39*, 1–7.
- Shearer, P. (2000), Upper mantle seismic discontinuities, in *Earth's Deep Interior: Mineral Physics and Tomography From the Atomic to the Global Scale*, *Geophys. Monogr. Ser.*, vol. 117, edited by S. Karato et al., pp. 115–131, AGU, Washington, D.C.
- Shen, W., M. Ritzwoller, V. Schulte-Pelkum, and F.-C. Lin (2013a), Joint inversion of surface wave dispersion and receiver functions: A Bayesian Monte-Carlo approach, *Geophys. J. Int.*, *192*, 807–836.
- Shen, W., M. Ritzwoller, and V. Schulte-Pelkum (2013b), A 3-d model of the crust and uppermost mantle beneath the central and western US by joint inversion of receiver functions and surface wave dispersion, *J. Geophys. Res.*, *60*, 1–15, doi:10.1029/2012JB009602.
- Shen, X., H. Zhou, and H. Kawakatsu (2008), Mapping the upper mantle discontinuities beneath China with teleseismic receiver functions, *Earth Planets Space*, *60*, 713–719.

- Shen, Y., and J. Blum (2003), Seismic evidence for accumulated oceanic crust above the 660-km discontinuity beneath southern Africa, *Geophys. Res. Lett.*, *30*, 1–4.
- Sigloch, K., N. McQuarrie, and G. Nolet (2008), Two-stage subduction history under North America inferred from multiple-frequency tomography, *Nat. Geosci.*, *1*, 458–462.
- Simmons, N. A., and H. Gurrrola (2000), Multiple seismic discontinuities near the base of the transition zone in the Earth's mantle, *Nature*, *405*, 559–562.
- Smyth, J., and S. Jacobsen (2006), Nominally anhydrous minerals and Earth's deep water cycle, in *Earth's Deep Water Cycle*, vol. 167, edited by S. Jacobsen and S. van der Lee, pp. 1–9, AGU monograph, AGU, Washington, D. C.
- Song, T., D. Helmberger, and S. Grand (2004), Low-velocity zone atop the 410-km seismic discontinuity in the northwestern United States, *Nature*, *427*, 530–533.
- Stixrude, L., and C. Lithgow-Bertelloni (2005), Mineralogy and elasticity of the oceanic upper mantle: Origin of the low-velocity zone, *J. Geophys. Res.*, *110*, 1–16.
- Stixrude, L., and C. Lithgow-Bertelloni (2007), Influence of phase transformations on lateral heterogeneity and dynamics in Earth's mantle, *Earth Planet. Sci. Lett.*, *263*, 45–55.
- Sun, D., and D. Helmberger (2011), Upper-mantle structures beneath USArray derived from waveform complexity, *Geophys. J. Int.*, *184*, 416–438.
- Tauzin, B., E. Debayle, and G. Wittlinger (2008), The mantle transition zone as seen by global Pds phases: No clear evidence for a thin transition zone beneath hot spots, *J. Geophys. Res.*, *113*, 1–17.
- Tauzin, B., E. Debayle, and G. Wittlinger (2010), Seismic evidence for a global low velocity layer within the Earth's upper mantle, *Nat. Geosci.*, *3*, 718–721.
- Vacher, P., A. Mocquet, and C. Sotin (1998), Computation of seismic profiles from mineral physics: The importance of the non-olivine components for explaining the 660 km depth discontinuity, *Phys. Earth Planet. Inter.*, *106*, 275–298.
- van der Meijde, M., F. Marone, D. Giardini, and S. van der Lee (2003), Seismic evidence for water deep in Earth's upper mantle, *Science*, *300*, 1556–1558.
- van Keken, P., S. Karato, and D. Yuen (1996), Rheological control of oceanic crust separation in the transition zone, *Geophys. Res. Lett.*, *23*, 1821–1824.
- Vinnik, L., and V. Farra (2007), Low velocity atop the 410-km discontinuity and mantle plumes, *Earth Planet. Sci. Lett.*, *262*, 398–412.
- Vinnik, L., Y. Ren, E. Stutzmann, V. Farra, and S. Kiselev (2010), Observations of S410p and S350p phases at seismograph stations in California, *J. Geophys. Res.*, *115*, 1–12, doi:10.1029/2009JB006582.
- Weidner, D., and Y. Wang (1998), Chemical- and Clapeyron-induced buoyancy at the 660 km discontinuity, *J. Geophys. Res.*, *103*, 7431–7441.
- Weidner, D., and Y. Wang (2000), Phase transformations: Implications for mantle structure, in *Earth's Deep Interior: Mineral Physics and Tomography From the Atomic to the Global Scale*, *Geophys. Monogr. Ser.*, edited by S. Karato et al., pp. 215–235, AGU, Washington, D.C.
- West, J., M. Fouch, J. Roth, and L. Elkins-Tanton (2009), Vertical mantle flow associated with a lithospheric drip beneath the Great Basin, *Nature*, *2*, 439–444.
- Wittlinger, G., and V. Farra (2007), Converted waves reveal a thick and layered tectosphere beneath the Kalahari super-craton, *Earth Planet. Sci. Lett.*, *254*, 404–415.
- Wittlinger, G., J. Vergne, P. Tapponnier, V. Farra, G. Poupinet, M. Jiang, H. Su, G. Herquel, and A. Paul (2004), Teleseismic imaging of subducting lithosphere and Moho offsets beneath western Tibet, *Earth Planet. Sci. Lett.*, *221*, 117–130.
- Wood, B. (1995), The effect of H₂O on the 410-kilometer seismic discontinuity, *Science*, *268*, 74–76.
- Xu, W., C. Lithgow-Bertelloni, L. Stixrude, and J. Ritsema (2008), The effect of bulk composition and temperature on mantle seismic structure, *Earth Planet. Sci. Lett.*, *275*, 70–79.
- Zandt, G., and E. Humphreys (2008), Toroidal mantle flow through the western U.S. slab window, *Geology*, *36*, 295–298.
- Zhu, L. (2000), Crustal structure across the San Andreas fault, southern California, from teleseismic converted waves, *Earth Planet. Sci. Lett.*, *179*, 183–190.
- Zoback, M., R. Anderson, and G. Thompson (1981), Cainozoic evolution of the state of stress and style of tectonism of the Basin and Range province of the western United States, *Phil. Trans. Soc. Lon.*, *300*, 407–434.